

PAPER

## Robust real-time feedback algorithms for plasma kinetic control in advanced tokamak scenarios

To cite this article: S Wang *et al* 2021 *Plasma Phys. Control. Fusion* **63** 125001

View the [article online](#) for updates and enhancements.

### You may also like

- [Fabrication of intermetallic NiAl by self-propagating high-temperature synthesis reaction using aluminium nanopowder under high pressure](#)  
Shushan Dong, Ping Hou, Haiyong Cheng *et al.*
- [Simulation Study on Laser Damage of Iron Plate](#)  
Tianyu Wang, Jintian Bian, Qing Ye *et al.*
- [Modelling and application of a new method to measure the non-thermal electron current in the edge of magnetically confined plasma](#)  
Shaocheng Liu, Yunfeng Liang, Huaxiang Zhang *et al.*



**IOP | ebooks™**

Bringing together innovative digital publishing with leading authors from the global scientific community.

Start exploring the collection—download the first chapter of every title for free.

# Robust real-time feedback algorithms for plasma kinetic control in advanced tokamak scenarios

S Wang<sup>1,\*</sup> , D Moreau<sup>2</sup>, E Witrant<sup>1</sup> , J P Qian<sup>3</sup>, Q P Yuan<sup>3</sup> , Y Huang<sup>3</sup>, L Zeng<sup>3</sup>   
and the EAST Team

<sup>1</sup> Université Grenoble Alpes, CNRS, GIPSA-lab, 38400 Grenoble, France

<sup>2</sup> CEA, IRFM, 13108 Saint-Paul-lez-Durance, France

<sup>3</sup> Institute of Plasma Physics, Chinese Academy of Sciences, Hefei 230031, Anhui, People's Republic of China

E-mail: [sen.wang1@gipsa-lab.fr](mailto:sen.wang1@gipsa-lab.fr)

Received 23 June 2021

Accepted for publication 20 September 2021

Published 18 October 2021



## Abstract

Robust real-time control algorithms for tracking plasma kinetic parameters in advanced tokamak scenarios are developed based on linear state-space (LSS) dynamic models. The real-time control algorithms under study comprise the  $\mathcal{H}_\infty$  robust control, the linear quadratic integral control and the internal model control. The plasma models used in this work are restricted to LSS models identified from dedicated simulation/experimental data, though the proposed control algorithms can conveniently be extrapolated to broadly incorporate linear models obtained from first-principles plasma theory. The control objective is to track plasma kinetic parameters of interest to desired operating points in advanced tokamak scenarios by actuating additional heating & current drive systems in real-time. Plasma kinetic parameters involve the poloidal pressure parameter  $\beta_p$ , the internal inductance  $l_i$ , the average toroidal rotation angular speed  $\Omega_\phi$  and the electron temperature on axis  $T_{e,0}$  while the actuators are the ion cyclotron resonance heating and lower hybrid current drive systems. In order to achieve enhanced control performance, two control layers are designed. The outer layer, i.e. an internal model-based proportional-integral actuator controller, operating on a fast timescale ( $\ll$  the energy confinement time  $\tau_E$ ) aiming at tracking the commands requested by the inner kinetic controllers, while the inner layer, i.e. a kinetic controller chosen from various alternatives, running on a slow timescale ( $\sim \tau_E$ ) is dedicated to tailoring plasma kinetic parameters. Simulation results for the experimental advanced superconducting tokamak (EAST) tokamak are provided and compared to show the capabilities of each control approach. Dedicated kinetic control experiments conducted in an H-mode scenario on EAST are reported as well. The advantages and limits of these control algorithms are discussed and summarised.

Keywords: plasma control, advanced tokamak scenarios, plasma kinetic parameters, additional heating and current drive

(Some figures may appear in colour only in the online journal)

\* Author to whom any correspondence should be addressed.

## 1. Introduction

The exploitation of controlled thermonuclear fusion is widely believed to be a potential dominant energy solution to powering our Earth because, in addition to the abundant nuclear fusion fuels in nature, it exhibits strong and stable fusion power intensities, without generating harmful long-lasting nuclear wastes [1, 2]. Among all the proposed thermonuclear fusion concepts, the tokamak is the most promising one, primarily due to the enhanced plasma confinement enabled by its high toroidal magnetic field and plasma current. In order to extract nuclear fusion energy for electricity production, it is crucial to operate tokamak devices in advanced scenarios, characterized by high plasma temperatures, densities and long energy confinement time, with a large fraction of plasma current self-generated from the bootstrap effect [3–5]. In view of the presence of various plasma disturbing phenomena, for example, some deleterious magnetohydrodynamic instabilities and microturbulence [1], it is necessary to develop some state-of-the-art feedback control schemes to reproducibly achieve and maintain the desired advanced tokamak scenarios.

The significance of active control of advanced tokamak scenarios has attracted sufficient attention in the tokamak fusion community. In recent years, numerous control schemes have emerged for tailoring plasma magnetic and kinetic parameters/profiles. Apart from a few empirical-based proportional controllers, the majority of them are synthesized from control-oriented plasma dynamic models, either using first-principles-driven dynamic models [6] or linear data-driven models [7, 8], either using the early lumping approach (i.e. discretize-then-design) [9] or the late lumping approach (i.e. design-then-discretize) [10]. Normally these feedback control algorithms are assessed numerically and/or experimentally, at least, in a specific plasma scenario of interest on one tokamak device. The proposed control techniques comprise simple proportional-integral-derivative (PID) control [11, 12], linear-quadratic-integral (LQI) control [13, 14],  $\mathcal{H}_\infty$  robust control [15, 16], model predictive control [17–19], passivity-based control [20], Lyapunov-based control [21–23] and adaptive control [24]. More precisely, in [11], a simple PID controller is designed to control the central safety factor using the lower hybrid waves on the Joint European Torus (JET) tokamak. In [13], an LQI optimal controller is combined with a nonlinear input transformation to minimize the weighted norm of tracking errors and control efforts in L-mode plasmas on DIII-D. In [18], a model-predictive controller is developed to track the safety factor profile and plasma  $\beta$ , defined as the ratio between the volume-averaged pressure and the magnetic pressure, that accounts for the time-varying operational and physics limits and is tested experimentally in L-mode plasmas on the Tokamak à Configuration Variable (TCV) tokamak. In [20], the interconnection and damping-assignment passivity-based control is developed and evaluated experimentally in L-mode plasmas on TCV. In [22], a Lyapunov-based infinite dimensional controller for the safety factor profile combined with simple internal model control with proportional-integral structure (SIMC PI) for  $\beta$  is validated both numerically and

experimentally in a TCV L-mode plasma. An infinite dimensional controller was also obtained for the nonlinear control of temperature profiles in H-mode scenarios in [23].

Even though a large number of real-time feedback control schemes have been proposed to track plasma magnetic and kinetic parameters in tokamaks, we find that performance comparison of different feedback controllers rarely appears in the literature, especially in advanced H-mode scenarios for which the models are at most highly uncertain and the physics is not well known. In this study, we make the first attempt to provide practical and valuable designs along this line. Specifically, we develop a set of popular finite-dimensional kinetic controllers based on the same linear time-invariant (LTI) data-driven model, and then evaluate and compare their performance and robustness by carrying out nonlinear closed-loop simulations and dedicated plasma experiments. A two-layer two-time-scale kinetic control scheme is thus developed for the comparative study, including an inner-layer with a low sampling frequency aimed at plasma kinetic control, whilst the high sampling frequency outer-layer deals with measurement preprocessing and actuation tracking. Three alternative finite-dimensional feedback controllers are introduced for the inner layer, namely  $\mathcal{H}_\infty$  robust control, LQI control and internal model control (IMC) control. The SIMC PI controller is also used to ensure that the actuators effectively deliver the input requested by the inner control layer. In addition, the plasma parameters of interest, experimentally reconstructed or measured by the real-time equilibrium code, P-EFIT [25], using magnetic measurements, as well as the coupled power measurements are handled by a set of average horizon filters in real-time for noise removal.

The experimental advanced superconducting tokamak (EAST) is a medium-sized fully superconducting D-shape tungsten divertor tokamak, with its major radius of 1.82 m, a minor radius of 0.45 m, and its elongation ranging from 1.5 to 2.0. One major scientific objective of this machine is to achieve and maintain long pulse high performance high bootstrap current operation, which appears as an ideal test-bed to evaluate and compare our real-time kinetic control algorithms. We emphasize that even though all the simulations and experiments carried out in this work are applied to specific operational scenarios on the EAST tokamak, the systematic procedures adopted in these control algorithms allow us to straightforwardly extend them to kinetic control in other tokamak plasma scenarios and devices. The conclusions obtained from performance comparison can provide us with valuable indications on the tricks and pitfalls of the use of each kinetic control algorithms.

The remainder of the article is organized as follows. Section 2 presents a linear state-space (LSS) model for plasma feedback controller design. In section 3, we propose a two-layer two-time-scale kinetic control scheme, including a number of alternative kinetic control algorithms, measurement preprocessing module and cascade actuation controllers. The performance of the feedback control scheme is assessed, discussed and compared numerically with the METIS plasma simulator [26] in section 4. Section 5 reports the initial experimental results obtained on the EAST tokamak.

Finally, in section 6 we draw the conclusions and outline possible extensions.

## 2. Plasma dynamic model for control

In this section, we first introduce a linear two-time-scale model structure to characterize the plasma dynamics in an H-mode operational scenario on the EAST tokamak. Subsequently, a model reduction technique based on the input lowpass filtering and singular value decomposition (SVD) is employed onto this plasma model for integrated feedback controller design.

### 2.1. Two-time-scale plasma model

The dynamic evolutions of plasma kinetic parameters with respect to control actuators, e.g. the lower hybrid current drive (LHCD) and the ion cyclotron resonance heating (ICRH) powers, in medium-sized or large tokamaks can be characterized by a lumped-parameter LTI two-time-scale model structure as demonstrated in [7, 14, 27, 28]. This dynamic model comprises a slow sub-model illustrating the slow responses of plasma kinetic parameters with respect to the poloidal magnetic fluxes as:

$$\begin{aligned} \dot{X}_\Psi(t) &= A_S X_\Psi(t) + B_S U_S(t) \\ \Xi_S(t) &= C_S X_\Psi(t) + D_S U_S(t) \end{aligned} \quad (1)$$

and a fast sub-model depicting the fast plasma kinetic evolutions possibly arising from plasma temperature profile variations as:

$$\begin{aligned} \dot{X}_F(t) &= A_F X_F(t) + B_F U_F(t) \\ \Xi_F(t) &= C_F X_F(t) + D_F U_F(t) \end{aligned} \quad (2)$$

in which

$$\begin{aligned} U(t) &= U_S(t) + U_F(t), \Xi(t) = \Xi_S(t) + \Xi_F(t) \\ U(t) &\stackrel{\text{def}}{=} U_0(t) - \bar{U}, \Xi(t) \stackrel{\text{def}}{=} \Xi_0(t) - \bar{\Xi}. \end{aligned} \quad (3)$$

Here,  $U(t)$  is defined as a perturbing vector of the control inputs  $U_0(t)$  around their input reference  $\bar{U}$ , with its slow and fast components denoted by  $U_S(t)$  and  $U_F(t)$ , respectively. Analogously,  $\Xi(t)$  is defined as a perturbing vector of the plasma kinetic parameters of interest  $\Xi_0(t)$  around their reference  $\bar{\Xi}$ , comprising its slow part as  $\Xi_S$  and its fast part as  $\Xi_F$ .  $X_\Psi(t)$  represents a perturbing vector of the poloidal magnetic fluxes against their reference values, while  $X_F(t)$  is a perturbed kinetic state vector. The state-space matrices  $(A_S, B_S, C_S, D_S)$  and  $(A_F, B_F, C_F, D_F)$  contain the model coefficient matrices, which can either be identified by using subspace and prediction-error approaches [29] or be obtained by performing linearization and discretisation on the sophisticated partial differential equations governing the plasma transport evolution. The approaches for obtaining these model coefficient matrices are beyond the scope of this article and interested readers can refer to [14, 27, 29] for more details.

### 2.2. Model reduction for integrated kinetic control design

We are now in a position to show that the linear two-time-scale plasma model [14] with equations (1)–(3) can be transformed into a compact form suitable for integrated feedback controller design. A lowpass filter is applied on the perturbed control inputs  $U(t)$  with the filter characteristic time  $\tau_{\text{filt}}$  satisfying  $\tau_{\text{kin}} \ll \tau_{\text{filt}} \ll \tau_{\text{mag}}$ , where  $\tau_{\text{kin}}$  and  $\tau_{\text{mag}}$  represent the kinetic and magnetic characteristic times, respectively. After some algebraic manipulations, the two-time-scale plasma model is therefore augmented into a state-space form as:

$$G = \left[ \begin{array}{c|c} A & B \\ \hline C & D \end{array} \right] \quad (4)$$

where

$$\begin{aligned} A &= \begin{bmatrix} A_S & 0 & B_S \\ 0 & A_F & -B_F \\ 0 & 0 & C_F A_F C_F^{-1} I \end{bmatrix} \\ B &= \begin{bmatrix} 0 \\ B_F \\ C_F B_F I \end{bmatrix} \\ C &= [C_S \quad C_F \quad D_S] \\ D &= 0. \end{aligned} \quad (5)$$

Here,  $(A_f, B_f, C_f, D_f)$  is a state-space realization of the low-pass filter  $G_f = \frac{1}{\tau_{\text{filt}} s + 1}$ , in which  $s$  is a Laplace operator. We note that, in equation (5), the symbols 0 and  $I$  represent the zero and identity matrices with appropriate dimensions, respectively.

When the controlled degrees of freedom are greater than the number of control actuators, the system is called an underactuated system [30], which is usually the case for tokamak plasma kinetic control. In this regard, minimizing the tracking error to zero may not be possible unless the given reference targets are located in an achievable region. Before synthesizing a feedback controller for an underactuated system, it is necessary to examine which output and input directions are most influential [15]. We therefore perform the SVD [31] of the steady-state gain matrix of the model  $G(s)$  to extract the most influential input and output control channels. In particular, to weigh the importance of each controlled outputs and manipulated inputs, symmetric positive definite matrices  $Q$  and  $R$  are first multiplied by the output and input of the model  $G(s)$ , generating a weighted dynamic model  $G_w(s) = Q^{\frac{1}{2}} G(s) R^{\frac{1}{2}}$ . Subsequently, we perform the SVD of the steady-state gain matrix of the weighted model, yielding  $G_w(0) = U_0 \Sigma_0 V_0^T$ .  $\Sigma_0 = \text{diag}\{\Sigma_I, \Sigma_{II}\}$  is a diagonal matrix with the singular values in a descending order as  $\sigma_1 \geq \sigma_2 \geq \dots \geq \sigma_{n_I} \gg \sigma_{n_I+1} \gg \dots \gg \sigma_{n_d}$ ,  $n_d = \min\{n_y, n_u\}$ , with  $n_y$  and  $n_u$  respectively denoting the number of outputs (controlled kinetic variables) and inputs (control actuators).  $\Sigma_I$  contains the largest  $n_I$  singular values while  $\Sigma_{II}$  contains the remaining insignificant ones. The left singular vectors  $U_0 = [U_I, U_{II}] \in \mathbb{R}^{n_y \times n_u}$  are divided into the level I and II vector spaces, in which the level I singular vectors represent the most controllable output directions. Likewise,  $V_0 = [V_I, V_{II}] \in \mathbb{R}^{n_u \times n_u}$  have the first  $n_I$  columns retained,

as they correspond to the most influential input directions  $V_1$ . We remark that  $Q$  and  $R$  are the weighting gain matrices that can be iteratively adjusted to reach various control objectives. The decision on the restricted number of retained control channels  $n_I$  is heuristic, which can empirically be determined by following the condition  $\sigma_{n_I+1} \leq 0.1\sigma_1$ . With such a procedure, the integrated plasma model  $G(s)$  can thus be transformed into a reduced one, which is proper, stabilizable and detectable. The reduced model is therefore given by  $G_r(s) = M_y^T G(s) M_u$ , where  $M_y = U_1^T$  and  $M_u = V_1 \Sigma_1^{-1}$ , and its state-space form can be expressed as:

$$G_r(s) = \begin{bmatrix} A_r & B_r \\ C_r & D_r \end{bmatrix}. \quad (6)$$

### 3. Robust linear feedback algorithms

Having obtained a control-oriented state-space plasma dynamic model, linear real-time kinetic feedback control algorithms can immediately be synthesized. An overall control architecture for plasma kinetic control is first presented. Subsequently, a number of alternative kinetic feedback algorithms are developed based on the same kinetic model, along with some beneficial techniques for measurement preprocessing and control actuation tracking.

#### 3.1. Two-layer cascade kinetic control framework

As shown in figure 1, the overall kinetic feedback control framework for the EAST tokamak comprises two control layers that differ in the sampling frequency. The inner control layer, within the dashed purple frame, has a low sampling frequency at 50 Hz. It contains a set of alternative kinetic controllers such as the  $\mathcal{H}_\infty$  robust control, the LQI control and the IMC control, along with a switch for real-time controller selection. Details on the design of these kinetic controllers are given in section 3.2 and appendices A–C. The outer control layer, within the green frame but outside of the purple one, has a higher sampling frequency at 1000 Hz. It is primarily devoted to two separate tasks: (a) to preprocess the measured actuations from relevant actuator sensors and the real-time estimates of the plasma parameters of interest after the EFIT equilibrium reconstruction [32–34]; (b) to track the actuator commands requested by a selected inner-layer kinetic controller. Cascaded with an inner-layer kinetic controller, the actuation controller is designed for actuation tracking, as illustrated in appendix D. In the measurement preprocessing module, a set of simple average horizon filters [29] can be used to handle the high-frequency noise in the measured outputs. Following the same technique as in [35], the anti-windup module is designed to mitigate the effects from the actuator saturations. We remark that the idea of the two-layer kinetic control framework arises from the following facts: (a) the time constant of the actuator dynamics such as the LHCD system is much smaller than the energy confinement time on EAST. (b) Plasma model uncertainties located in the high frequency

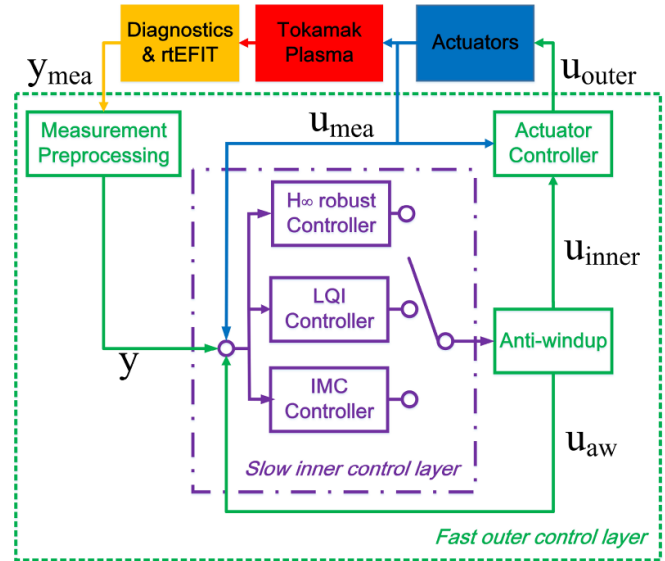


**Figure 1.** Layout of the two-layer cascade kinetic control framework.

domain beyond  $\tau_E$  are not likely to damage the tracking performance if we properly prescribe the inner-layer sampling time to the level a few times smaller than  $\tau_E$  [29]. (c) The inner-layer kinetic controller can greatly benefit from the precise tracking of the requested commands enabled by the outer-layer actuation controller within one inner-layer sampling interval.

#### 3.2. Linear feedback control algorithms

In this section, linear feedback control algorithms are presented, including  $\mathcal{H}_\infty$  robust control, LQI control, IMC control and SIMC PI control.

$\mathcal{H}_\infty$  robust control is a popular feedback control technique whose synthesis combines  $\mathcal{H}_\infty$  robust stabilization with loop-shaping [31]. Basically, the design procedure is composed of two steps: (a) to augment the pre- and post-compensators on an open-loop system plant to acquire an expected singular value shaping in the frequency-domain; (b) to synthesize a feedback controller by making the augmented system plant robust against model uncertainties with the  $\mathcal{H}_\infty$  norm optimization. Thanks to its simplicity and robustness properties, it has been applied to real-time feedback of magnetic and kinetic parameters in tokamak plasmas. In [15], the robust synthesis based on a first-principle-driven dynamic model for  $q$ -profile control was experimentally tested in L-mode plasmas on DIII-D. In [36],  $\mathcal{H}_\infty$  robust control was applied to plasma coil current and shape control on WEST experimentally. In [35], the performance of a decentralized  $\mathcal{H}_\infty$  robust controller for the  $q$ -profile and  $\beta_p$  tracking on EAST is assessed numerically. In the present study, we adopt a similar synthesis method as in [35], but extend its application scope to multiple kinetic parameters and experimental setups. Another subtle difference is that in the present work, a single  $\mathcal{H}_\infty$  robust controller is

designed based on an integrated kinetic model containing both the fast and slow kinetic dynamics. Given the reduced model  $G_r(s)$ , the design of an  $\mathcal{H}_\infty$  robust controller is detailed in appendix A.

LQI control, a linear optimal control technique [31], extends the traditional linear quadratic regulator to involve the penalization of the control error integral in the cost function, with the goal of achieving a zero steady-state tracking error under constant disturbances. This technique was first proposed in [37], has then been applied to many industrial and physical control problems [38–41]. The merits of this technique are that it can be employed systematically for multiple-input multiple-output (MIMO) systems and that the controller performs satisfactorily in attenuating system disturbances. Notably, LQI has found its applications in many tokamak plasma control problems. In [7], LQI was used to track the poloidal flux profile and  $\beta_N$  simultaneously in H-mode plasmas on DIII-D. In [13], experimental tests have confirmed the performance of an LQI controller in tailoring the  $q$ -profile in an L-mode plasma on DIII-D. In [42], the snowflake divertor configuration is achieved numerically by an LQI controller on NSTX-U. In this study, we design an LQI controller using the reduced model  $G_r(s)$ , and compare its performance with other controllers. This control algorithm consists of a feedforward controller to estimate the input and state references, a Luenberger observer to estimate system states and a static feedback controller to compute the actuation commands. Appendix B illustrates the design of an LQI controller in great detail.

IMC is a robust control technique first proposed in [43]. The key idea of IMC resides in the internal model principle, stating that control can be achieved only if the control system involves, either implicitly or explicitly, some representation of the controlled process [44]. IMC has a simple design procedure providing a trade-off between closed-loop performance and robustness to model inaccuracies with a single tuning parameter, which explains why it has found widespread applications [45–47]. The concept of IMC has already been used in tokamak plasma control, of which a typical example is the design of an anti-windup compensator to handle the actuator saturations [35]. Nonetheless, a pivotal drawback of the standard IMC lies in its restrictive applicability to an internally stable system, implying that control of unstable plasma phenomena such as vertical instability [48] using IMC seems unfeasible. Inspired by [49], we develop an offset-free IMC control algorithm based on a PI observer for plasma kinetic tracking, which can potentially be adapted to control unstable and marginally stable plasma dynamics. The design of the observer-based IMC controller is composed of three steps: first, we use a PI Luenberger observer to estimate the states and disturbances. Second, we design a state feedback controller to stabilize the system dynamics. Third, a standard IMC control is adopted to achieve desirable control performance. Details on the IMC design procedure are provided in appendix C.

To mimic the experimental heating and current drive (H&CD) actuation in tokamak plasma operation, the actuator dynamics is taken into account and a set of actuator controllers are developed to track the commands requested by

the inner-layer kinetic controllers. In this study, the actuator dynamics for the H&CD systems is simply modelled as a set of first-order transfer functions with time-delay, whose parameters are identified from the sampled input–output data collected from dedicated plasma experiments using the prediction-error method [29]. A SIMC PI tuning rule is then adopted for each actuator feedback controller, as described in appendix D.

#### 4. Simulation results by the METIS code

We now demonstrate the effectiveness of the two-layer kinetic control scheme and assess the performance and robustness of the various real-time kinetic controllers on EAST using the minute embedded tokamak integrated simulator (METIS) code [26]. First, we show the performance of nominal tracking of three essential plasma kinetic parameters, namely the poloidal beta  $\beta_p$ , the average toroidal angular rotation velocity  $\Omega_\phi$  and the central electron temperature  $T_{e,0}$  by adjusting the ICRH power  $P_{ICRH}$  and the LHCD power  $P_{LHCD}$ , enabled by three optional kinetic controllers, i.e.  $\mathcal{H}_\infty$  robust, LQI and the observer-based IMC, and two SIMC PI power controllers for ICRH and LHCD. Second, robustness tests, under the variations of the line-averaged electron density  $\langle \bar{n}_e \rangle$  and effective ion charge  $Z_{\text{eff}}$ , are conducted and compared.

##### 4.1. METIS simulation setup and control configuration

The two-layer cascade control architecture is first developed and implemented in the MATLAB/Simulink environment, and is then coupled with a nonlinear tokamak plasma simulator METIS [26], for closed-loop control assessment. The reference scenario around which the model is identified is a steady state, fully non-inductive single-null H-mode discharge in the EAST tokamak, i.e. shot #62946, with the toroidal magnetic field  $B_T = 2.5$  T, the central electron density  $n_{e0} \approx 3.5 \times 10^{19} \text{ m}^{-3}$  and plasma current  $I_p = 0.42$  MA. More details about the METIS setup are given in [35]. The three alternative kinetic feedback control algorithms are designed and implemented based on a LSS model identified from extensive dedicated simulations via the subspace and prediction-error methods [29]. The actuators, the ICRH and LHCD powers, are allowed to vary in the ranges of [0, 1.5] and [0, 3.0] MW, respectively. As illustrated in figure 1, the plasma kinetic control scheme is separated into two control layers with two timescales: in the outer layer, the powers coupled to the plasma, from the ICRH and LHCD systems, are tracked on the fast timescale with the sampling frequency at 1 kHz; in the inner layer, the kinetic parameters are controlled simultaneously by one of the three alternative kinetic controllers on the slow timescale with the sampling frequency at 50 Hz (larger than  $\frac{1}{\tau_E}$ ). The actuator dynamics for the ICRH and LHCD systems are modelled by two separate first-order transfer functions with time-delay. Guided by the experimental data on EAST, the actuation time constants for the ICRH and LHCD systems are chosen to be 5 ms, and the effective time delay for the actuators is uniformly set at 2 ms, while the steady-state gains are prescribed to be

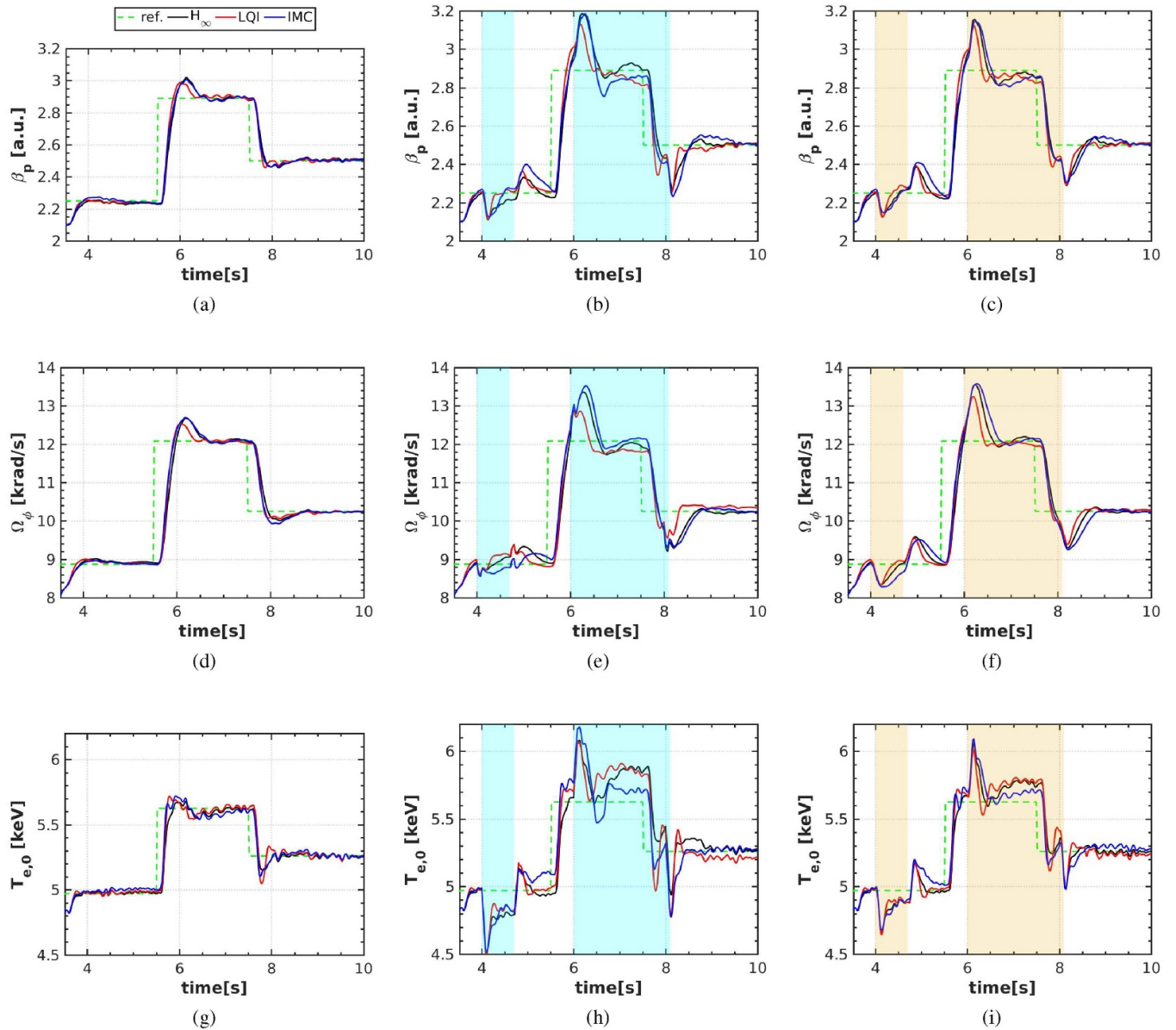


**Figure 2.** Tracking of plasma kinetic parameters with three alternative real-time feedback algorithms. Tracking of  $\beta_p$  (a),  $\Omega_\phi$  (d) and  $T_{e,0}$  (g) in the nominal case. Tracking of  $\beta_p$  (b),  $\Omega_\phi$  (e) and  $T_{e,0}$  (h) by perturbing  $\langle \bar{n}_e \rangle$ . Tracking of  $\beta_p$  (c),  $\Omega_\phi$  (f) and  $T_{e,0}$  (i) when perturbing  $Z_{\text{eff}}$ .

1. With these actuator dynamics models, two separate SIMC PI power controllers are thus synthesized, with  $\tau_{c,i} = 0.005$  s and  $\theta_i = 0.002$  s for both actuators ( $i \in \{\text{ICRH, LHCD}\}$ ). Note that the actuator control parameters can be adjusted according to the specific control requirements. In order to mimic the experimental conditions, white noise with power magnitude at  $10^{-6}$  is imposed onto the measured powers obtained from the simple actuator dynamics models. The noise is thus handled by a moving average filter with the time horizon at 10 ms. The three kinetic controllers were designed with the same linear reduced model. For the  $\mathcal{H}_\infty$  controller, a desired closed-loop bandwidth is prescribed to be  $0.15\pi$  Hz, and the parameters  $A$  and  $M$  are respectively set at 2 and  $10^{-6}$ . For the LQI controller, the weighting gains for the states, controlled variables and manipulated variables are optimized to achieve

the desired control performance. For the IMC controller, the tuning parameter, i.e. the time constant, of the low pass filter  $\tau_{\text{IMC}}$ , is prescribed at 0.08 s.

#### 4.2. Nominal tracking in the current flat-top phase

The three alternative control schemes were used to track  $\beta_p$ ,  $\Omega_\phi$  and  $T_{e,0}$  simultaneously by actuating the ICRH and LHCD powers. All the feedback controllers are activated at 3.5 s in the current flat-top phase. Three sets of reference setpoints for  $\beta_p$ ,  $\Omega_\phi$  and  $T_{e,0}$  are prescribed. Figures 2(a), (d) and (g) show the comparison of the kinetic parameter evolutions with the three alternative control algorithms. It is evident that all the kinetic controllers based on the same data-driven model are capable of tracking the plasma parameters of interest effectively

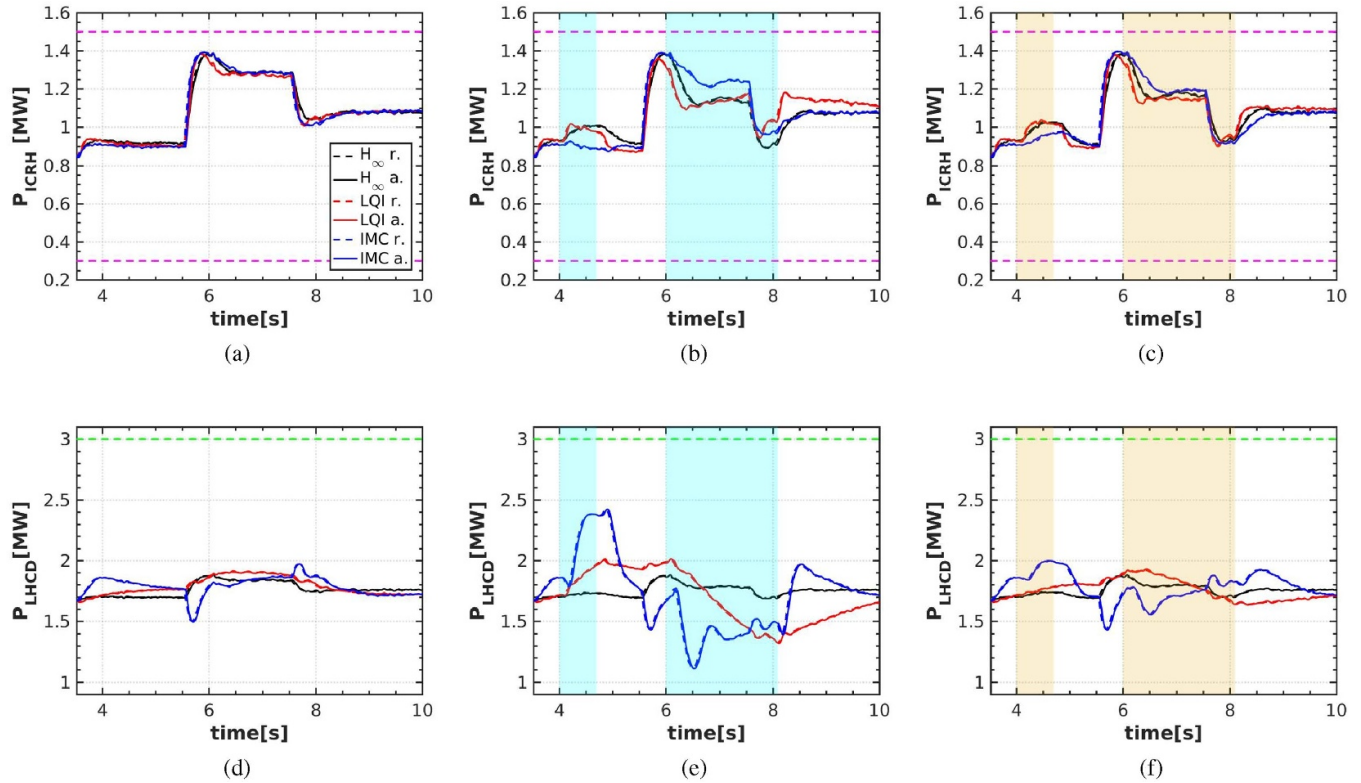


**Figure 3.** Tracking of the powers coupled to the plasma from the H&CD systems. (a)–(c) Time traces of the ICRH power request (dashed) and the actuated ICRH power (solid) with the  $\mathcal{H}_\infty$  (black), LQI (red) and IMC (blue) controllers in the nominal case (a), the perturbed  $\langle \bar{n}_e \rangle$  case (b) and the perturbed  $Z_{\text{eff}}$  case. (d)–(f) Time traces of the LHCD power request (dashed) and the actuated LHCD power (solid) with the  $\mathcal{H}_\infty$  (black), LQI (red) and IMC (blue) controllers when perturbing  $Z_{\text{eff}}$ .

and comparable control performance has been obtained. One can notice that there are some small oscillations even at steady-state for  $T_{e,0}$ , primarily due to the measurement noise imposed on  $P_{\text{ICRH}}$  and  $P_{\text{LHCD}}$ . Compared with the other kinetic parameters, the evolution of  $T_{e,0}$  is very sensitive to the additional heating powers. The powers requested (dashed) and actuated (solid) by the three controllers are shown in figures 3(a) and (d). We find that the SIMC PI power feedback controller can satisfactorily track the powers requested by the inner-layer kinetic controllers in the three cases. The requested ICRH powers are at similar levels in all the control schemes, but the LHCD powers differ, implying that the ICRH system plays the dominant role in the kinetic control for parameters that do not depend strongly on the current density profile such as  $\beta_p$ ,  $\Omega_\phi$  and  $T_{e,0}$ .

#### 4.3. Robustness to plasma parameter uncertainties

In order to further evaluate the robustness of each controllers, we performed closed-loop METIS simulations in which we perturbed a number of important plasma parameters at selected time intervals. Figures 2(b), (e) and (h) show a comparison of the kinetic parameter evolutions with the  $\mathcal{H}_\infty$ , LQI and IMC controllers under the perturbation of the averaged electron density. In the time interval [4.0, 4.65] s, the value of  $\langle \bar{n}_e \rangle$  is increased by 10%, which leads to the decrease of  $\beta_p$ ,  $\Omega_\phi$  and  $T_{e,0}$ . In order to attenuate the disturbances, the feedback

controllers request more powers on the ICRH and/or LHCD systems. Within 0.3 s the disturbances on  $\beta_p$  are fully compensated while the disturbances on  $\Omega_\phi$  and  $T_{e,0}$  are attenuated effectively. After 4.65 s,  $\langle \bar{n}_e \rangle$  returns to the initial value, which results in the increase of  $\beta_p$ ,  $\Omega_\phi$  and  $T_{e,0}$ . These new disturbances are successfully attenuated by the  $\mathcal{H}_\infty$  and LQI controllers, but not with the IMC controller. In the time interval [6.0, 8.1] s,  $\langle \bar{n}_e \rangle$  is artificially decreased by 10%, leading to the increase of the plasma parameters of interest. These  $\langle \bar{n}_e \rangle$ -driven disturbances on the controlled parameters are attenuated by decreasing the ICRH power except for  $T_{e,0}$  as shown in figures 3(b) and (e), because of the considerable model mismatch and the variation of the achievable control region in  $T_{e,0}$ . After 8.1 s,  $\langle \bar{n}_e \rangle$  returns to the initial value, the disturbances on  $\beta_p$ ,  $\Omega_\phi$  and  $T_{e,0}$  are successfully rejected by all the proposed control schemes.

Another comparison of the kinetic parameter evolutions with the proposed control algorithms under the perturbation of the effective ion charge are shown in figures 2(c), (f) and (i). Analogously, in the time interval [4.0, 4.65] s,  $Z_{\text{eff}}$  is artificially increased by 10%, which makes all the kinetic control variables drop. Results indicate that all the control schemes are capable of rejecting the disturbances arising from the  $Z_{\text{eff}}$  increase by adjusting the ICRH and LHCD powers (see figures 3(c) and (f)). In the time interval [6.0, 8.1],  $Z_{\text{eff}}$  is artificially reduced by 10%, which makes all the kinetic control variables increase. The simulation results suggest that all the

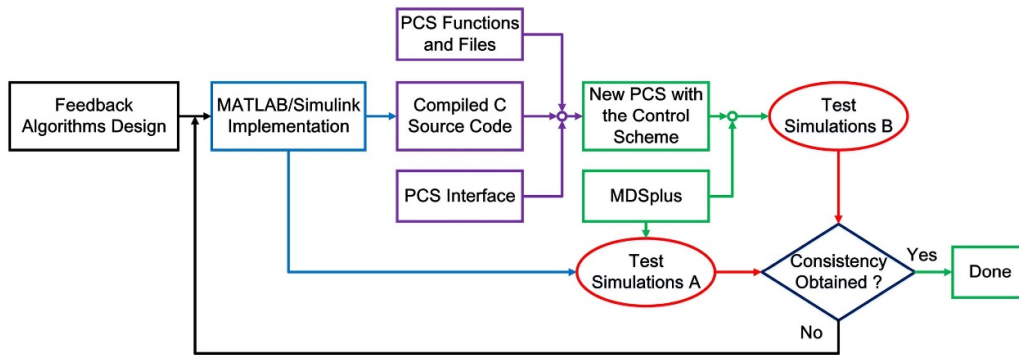


**Figure 4.** Diagram showing the procedure for the kinetic control algorithm implementation into the PCS.

controllers can fairly attenuate the disturbances caused by the  $Z_{\text{eff}}$  decrease, although the attenuation of the  $T_{e,0}$  disturbance driven by the  $Z_{\text{eff}}$  variation is not satisfactory in the period [6, 8] s, due to the presence of a large model mismatch.

## 5. Feedback control experiments on the EAST tokamak

In order to further evaluate and compare the performance of the proposed kinetic control schemes and algorithms, dedicated experiments have been performed in an H-mode operational scenario on the EAST tokamak, with the goal of tracking  $\beta_p$ , the internal inductance parameter  $li$  or the inverse of the plasma safety factor on the magnetic axis,  $\iota_0 = \frac{1}{q_0}$ , and the coupled LHCD power  $P_{\text{LHCD}}$  by adjusting the LHCD power command in real-time.

### 5.1. Control algorithm implementation in the PCS

Figure 4 shows how real-time feedback control algorithms can be implemented into the EAST plasma control system (PCS). We first develop the kinetic control algorithms in the MATLAB/Simulink environment, which are subsequently transformed into the C/C++ programming language using the embedded MATLAB coder (EMC) toolbox. Afterwards, the generated code is coupled with the PCS and jointly compiled for real-time application. The effectiveness of the algorithm implementation can be verified by performing test simulations via the EAST data simserver. Specifically, by feeding the same real-time EFIT estimates from a typical EAST plasma discharge to both versions of the kinetic control scheme, one implemented in MATLAB/Simulink and the other being coupled with the EAST PCS, the simulated outputs from both versions should be consistent with each other. This was checked, proving that no issues have appeared in the course of the control algorithm implementation in the PCS.

### 5.2. Diagnostics, actuators and experimental setup

Plasma parameters/profiles such as  $\beta_p$  and  $li$  are estimated by the GPU-accelerated real-time equilibrium reconstruction code, P-EFIT [25]. The POLarimeter-INTerferometer

diagnostic measures the plasma electron density [50], regulated in real-time by a dedicated PID controller in the PCS. Due to reliability issues with the polarimeter diagnostic, the internal poloidal field measurements were not available during these experiments for the P-EFIT reconstruction. Plasma current, position and shape were also regulated by another set of dedicated controllers in the PCS. The controlled parameters,  $\beta_p$ ,  $li$  and the coupled power  $P_{\text{LHCD}}$ , are fed to the kinetic control scheme every 1 ms (outer-layer sampling time) to generate a power command while the kinetic control algorithms are activated every 20 ms (inner-layer sampling time). The measurement noise is handled by a moving average filter with a time horizon of 10 ms [29]. The control actuator is the LHCD system at 4.6 GHz with coupled powers between 1.0 and 2.5 MW, tracked in real-time by a SIMC PI power feedback controller. We note that the minimum LHCD power is preset at 1.0 MW to guarantee that the plasma remains in H-mode, without any H-L/L-H transitions in the course of control. The LHCD power dynamics at 4.6 GHz is approximated by a first-order transfer function with time-delay (see equation (D.1)), whose coefficients are identified from typical experimental data on EAST. Given the model coefficients, a SIMC PI rule is then adopted, resulting in a set of LHCD power feedback control coefficients (see appendix D) as  $K_{p,\text{LHCD}} = 0.41$ ,  $K_{I,\text{LHCD}} = 343.69$  and  $u_{\text{offset,LHCD}} = -0.45$ , together with a static feedforward power  $K_{\text{ff}} = 1.38$  MW to enhance the transient performance. The LHCD power actuation time delays are dealt with by a Smith predictor, with the prediction model as  $G(z) = \frac{0.4141}{z-0.4307}$ , where  $z$  refers to the Z-transform, and the estimated pure time delay is 2 ms. The PCS power command to the LHCD system is restricted to the range from 1 to 3 MW. Hence, an anti-windup module [35] is used to cope with the LHCD power command saturation. All the control references and coefficients are prescribed offline and loaded into the PCS before performing the experiments.

In the experimental study, the current flat-top phase of a pure radio-frequency upper-single-null H-mode plasma discharge is considered as the reference scenario, with the toroidal field at 2.5 T, the plasma current at 350 kA, the central electron density at  $\sim 4.2 \times 10^{19} \text{ m}^{-3}$  and the central electron temperature at  $\sim 4 \text{ keV}$ . In addition to the 4.6 GHz LHCD power, some LHCD power is injected at 2.45 GHz for current drive in the plasma current ramp-up phase, specifically

0.6 MW in the period [0.95, 2.25] s. Moreover, 0.9 MW of feedforward ECRH power is actuated during the current flat-top phase (in the time interval [1.98, 7.91] s) from two gyrotrons at 140 GHz to heat the plasma and maintain it in H-mode. The ICRH system was not available during the entire experiments.

The kinetic feedback control experiments are divided into two stages: first, the identification experiment is carried out to collect a set of sampled data for identification of a plasma dynamic model used for feedback control design; second, the performance of the real-time control algorithms is demonstrated experimentally.

### 5.3. Plasma identification experiment

The LHCD power at 4.6 GHz was allowed to vary in real-time ranging from 1.0 to 2.5 MW and the dominant plasma kinetic eigenmode,  $\sim \frac{1}{\tau_E}$ , was estimated to be around  $25 \text{ s}^{-1}$ . In order to identify a relevant kinetic model, the first task was to design LHCD power reference waveforms that maximally excite the dominant magnetic and kinetic eigenmodes. Such waveforms are shown in figure 5, including chirping and pseudorandom binary sequence (PRBS) power modulations. Since the expected  $\tau_E$  was around 0.04 s, the dominant frequency bandwidth of the LHCD power references in both signals was therefore restricted to be less than  $157 \text{ rad s}^{-1}$ , as shown in figure 5. It is apparent that the PRBS power spectrum is over 0.5 in the entire bandwidth of [1, 157]  $\text{rad s}^{-1}$ , and above 10 when  $f$  is lower in  $30 \text{ rad s}^{-1}$ . In contrast, the chirping signal has a similar level of power spectrum when  $f < 30 \text{ rad s}^{-1}$ , but the amplitude decreases exponentially when  $f > 30 \text{ rad s}^{-1}$ . One can infer that the PRBS signal can better excite the plasma kinetic eigenmodes in the higher frequency bandwidth than the chirping signal, while magnetic eigenmodes can be excited in a similar level by these two signals. Using the SIMC PI power feedback controller as given in section 5.2, the open-loop power modulation experiment has been carried out on the EAST tokamak, with the results depicted in figure 6. Evidently, the chirping power reference, ranging from 1.0 to 2.5 MW, for the LHCD system was satisfactorily tracked in shot #93297 (see figure 6(a)), with the plasma parameters of interest  $\beta_p$ ,  $li$  and  $\iota_0$  sufficiently responsive as shown in figure 6(b). In particular,  $\beta_p$  ranges from 1.5 to 1.9,  $li$  spreads from 0.9 to 1.2, while  $\iota_0$  lies in the interval [0.3, 0.5]. It is found that both  $li$  and  $\iota_0$  exhibit unphysical linear downward drifts, because of the inaccuracy in the measurements that are transmitted from the magnetic probes mounted at the plasma boundary to the P-EFIT equilibrium reconstruction. We remark that in the interval [2.5, 3.5] s, the LHCD system at 4.6 GHz had an actuation fault, which explains why the LHCD power reference cannot be tracked accurately in this period. Figures 6(c) and (d) show another plasma power modulation discharge, with the PRBS power reference tracked using the same power feedback controller. One can notice that the responses of  $\beta_p$ ,  $li$  and  $\iota_0$  with respect to the LHCD power are subject to persistent excitation, which is ideal for model identification, but the systematic linear downward drifts occurring in  $li$  and  $\iota_0$  could bring some issues on their control.

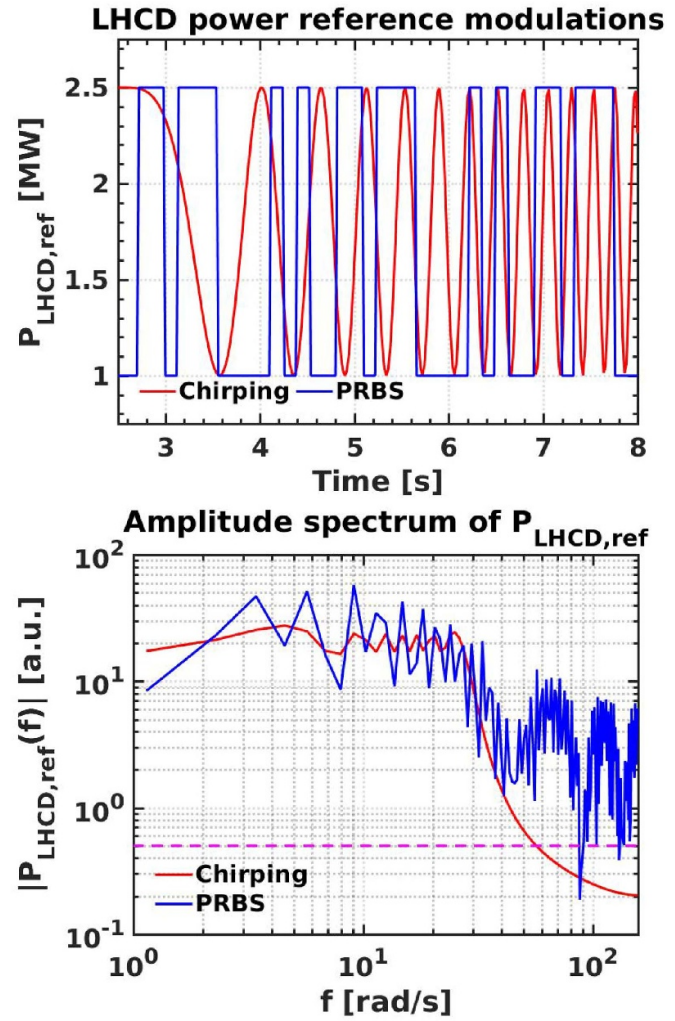


**Figure 5.** Design of LHCD power reference modulations to excite the dominant plasma eigenmodes. Upper panel: comparison of the  $P_{\text{LHCD,ref}}$  modulations in chirping (red) and PRBS (blue) signals. Bottom panel: comparison of the amplitude spectra of the  $P_{\text{LHCD,ref}}$  modulations in chirping (red) and PRBS (blue) signals.

### 5.4. Control assessment with the ARTAEMIS simulator

By adopting the system identification methodology used in [14, 27], a two-time-scale data-driven model that describes the responses of  $\beta_p$ ,  $li$  and  $\iota_0$  to the LHCD power has been identified from the power modulation data, containing five slow eigenmodes and one fast eigenmode [19]. More precisely, the characteristic times for the slow and fast dynamics are  $\tau_S = 1.05 \text{ s}$  and  $\tau_F = 0.017 \text{ s}$ , respectively. The identified two-time-scale model was then transformed into a standard LSS model by inserting a lowpass filter with  $\tau_{\text{filt}} = 0.1 \text{ s}$  at the control input. After model reduction, three alternative controllers are therefore designed using the reduced model. Table 1 lists the tuning parameters used for the design of the kinetic controller. The design of the IMC controller for each plasma kinetic parameters is performed separately by transforming the reduced model into a first-order transfer function with time delay ( $\theta = 20 \text{ ms}$ ). Prescribing the tuning parameter  $\tau_c = 4\theta$ , we therefore obtain the feedback coefficients  $K_p$  and  $K_i$  for

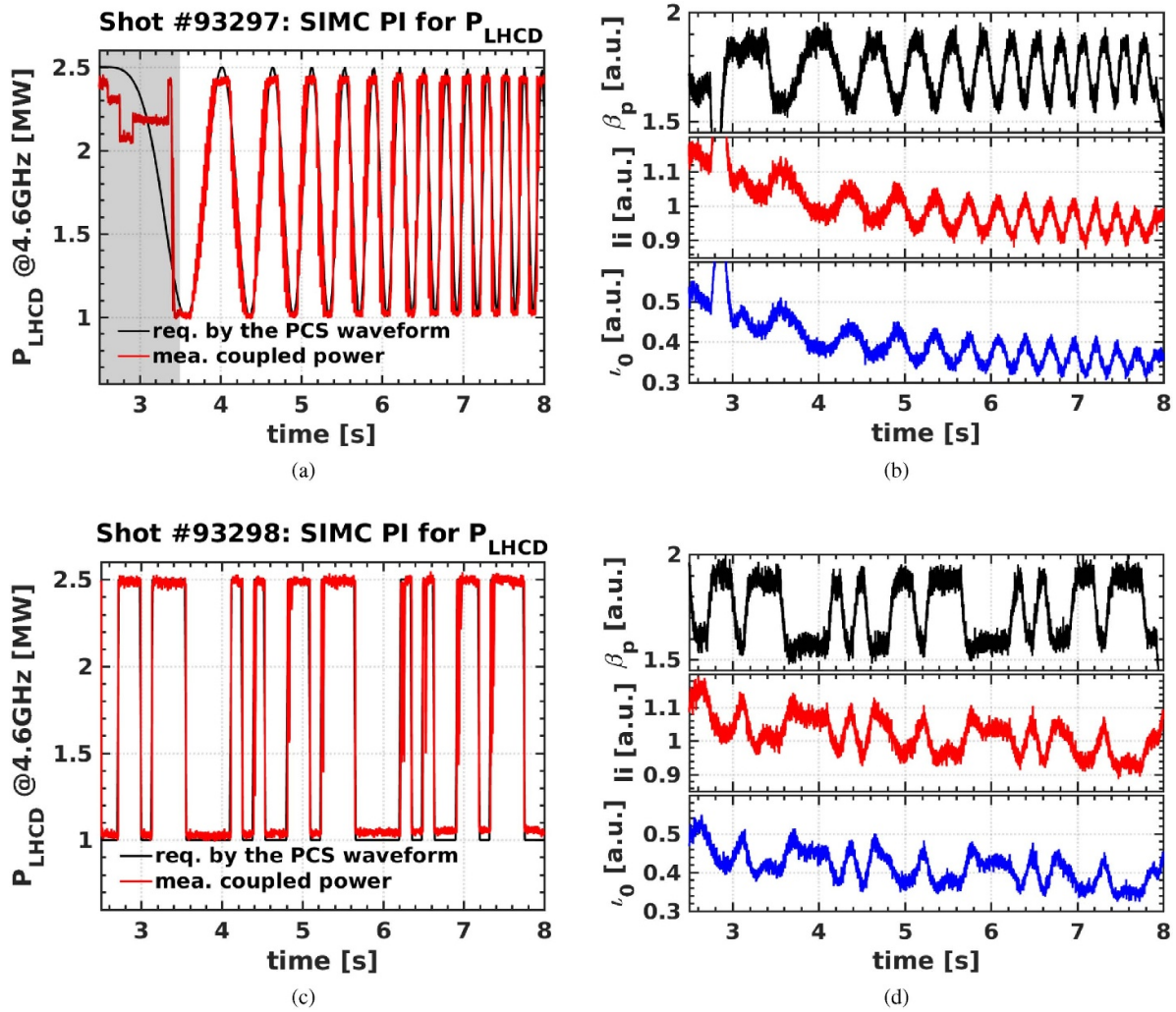


**Figure 6.** Plasma identification experiment showing the responses of  $\beta_p$ ,  $li$  and  $\nu_0$  to the  $P_{LHCD@4.6\text{ GHz}}$  modulations on EAST. Upper panels: time traces of (a) the  $P_{LHCD@4.6\text{ GHz}}$  modulations in a chirping frequency waveform, requested (black) and measured (red) after tracking by the SIMC PI power controller, and of (b)  $\beta_p$  (top),  $li$  (middle) and  $\nu_0$  (bottom) estimates by P-EFIT. Lower panels: time traces of (c) the  $P_{LHCD@4.6\text{ GHz}}$  modulations in a PRBS waveform, requested (black) and measured (red) after tracking by the SIMC PI power controller, and of (d)  $\beta_p$  (top),  $li$  (middle) and  $\nu_0$  (bottom) estimates by P-EFIT. The shaded gray region indicates that the LHCD system had faults and saturated.

**Table 1.** Tuning parameters for each kinetic controllers.

IMC	$K_p$	$K_i$	$G_{FF}$
$\beta_p$	2.05	53.99	5.40
$li$	-8.70	-142.30	-14.23
$\nu_0$	-11.47	-271.38	-27.14
$\mathcal{H}_\infty$	$M$	$\omega_b$	$A$
$\beta_p$	2	5.00	$10^{-6}$
$li$	2	2.00	$10^{-5}$
$\nu_0$	2	3.00	$10^{-6}$
LQI	$Q_s$	$Q_{o,int}$	$R$
$\beta_p$	1	700	0.1
$li$	1	4200	0.1
$\nu_0$	1	6000	0.02

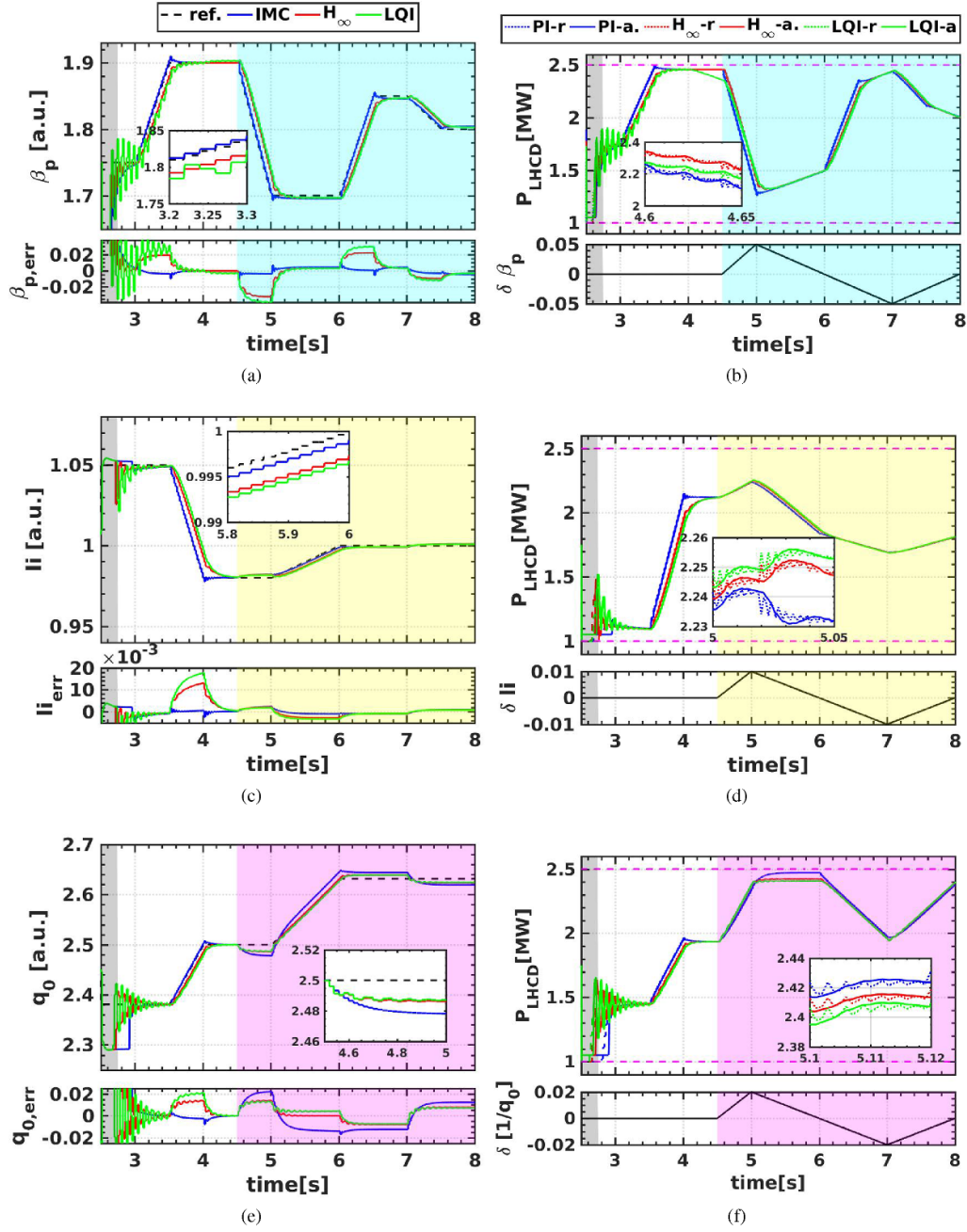


**Figure 7.** Simulated tracking of  $\beta_p$ ,  $li$  and  $q_0$  by actuating  $P_{\text{LHCD}}$  using the ARTAEMIS plasma simulator [27]. Top panels: time evolutions of ((a)-top)  $\beta_p$  and ((a)-bottom) its tracking error  $\beta_{p,\text{err}}$ , and of ((b)-top) the LHCD power  $P_{\text{LHCD}}$  and ((b)-bottom) virtual  $\beta_p$  disturbance,  $\delta\beta_p$ . Middle panels: time evolutions of ((c)-top)  $li$  and ((c)-bottom) its tracking error  $li_{\text{err}}$ , and of ((d)-top) the LHCD power  $P_{\text{LHCD}}$  and ((d)-bottom)  $li$  disturbance,  $\delta li$ . Bottom panels: time evolutions of ((e)-top)  $q_0$  and ((e)-bottom) its tracking error  $q_{0,\text{err}}$ , and of ((f)-top) the LHCD power  $P_{\text{LHCD}}$  and ((f)-bottom)  $q_0$  disturbance, denoted as  $\delta[1/q_0]$ . Shade regions imply the existence of disturbances. All feedback algorithms were activated at 2.75 s. The blue, red and green lines correspond to the simulation results of the IMC,  $\mathcal{H}_\infty$  and LQI control, respectively. On the left, dashed black lines denote control targets. On the right, the dotted lines represent the LHCD power targets requested by the kinetic controllers, while the solid lines are the achieved LHCD powers by a SIMC PI power controller.

$\beta_p$ ,  $li$  and  $\iota_0$ , respectively. The feedforward gain  $G_{\text{FF}}$  is computed by simply inverting the model coefficient  $k_i$  as given in equation (D.1). The design of the  $\mathcal{H}_\infty$  kinetic controller for each parameters is conducted subsequently, the weighting function  $K_S = \frac{s/M+w_b}{s+w_bA}$  is adjusted to shape the sensitivity functions, where the tuning of the closed-loop bandwidth  $\omega_b$  is essential to balance the control performance and robustness.

Finally, the design of the LQI kinetic controller for  $\beta_p$ ,  $li$  and  $\iota_0$  is carried out, in which the tuning parameters  $Q_s$ ,  $Q_{o,\text{int}}$  and  $R$  weigh the importance of the states, the output error integrals and the controlled inputs, respectively, in the cost function  $J_{\text{fb,LQI}}$  defined in equation (B.3). One can notice that the primary weights are put on the output error integrals to enable the transient control performance.

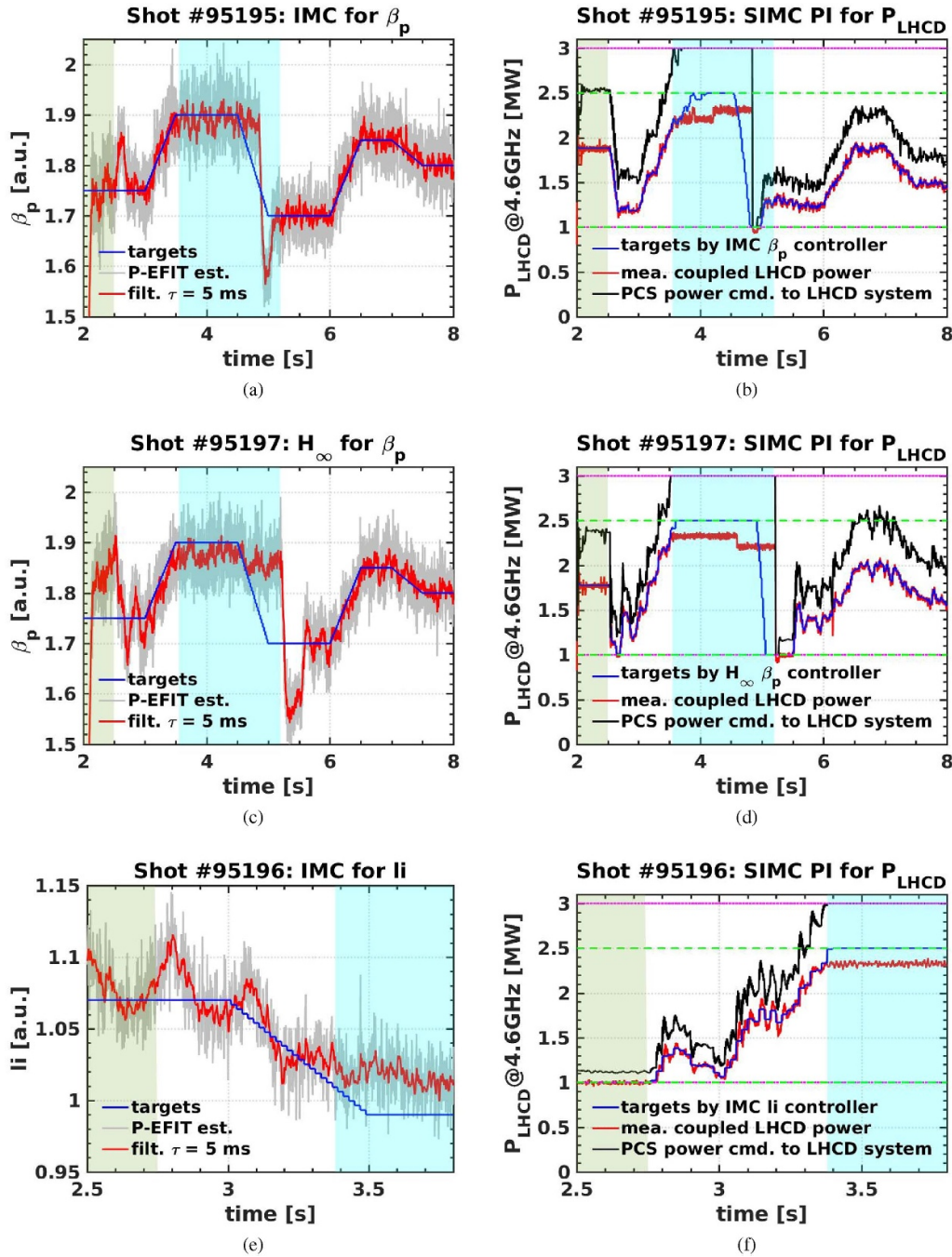


**Figure 8.** Plasma control experiments showing the tracking of  $\beta_p$  and  $li$  using the LHCD@4.6 GHz power command on EAST. Upper and middle panels: time traces of ((a), (c))  $\beta_p$  targets (blue), P-EFIT estimate (gray) and lowpass filtered P-EFIT estimate (red), and of ((b), (d)) the requested  $P_{\text{LHCD}@4.6\text{GHz}}$  (blue), the measured  $P_{\text{LHCD}@4.6\text{GHz}}$  (red) and the PCS power command to the LHCD system (black).  $\beta_p$  control was activated after 2.5 s right after the shaded light brown region. Bottom panels: time traces of  $li$  targets (blue), P-EFIT estimate (gray) and lowpass filtered P-EFIT estimate (red) and of the requested  $P_{\text{LHCD}@4.6\text{GHz}}$  (blue) and the measured  $P_{\text{LHCD}@4.6\text{GHz}}$  (red) and the PCS power command to the LHCD system (black).  $li$  feedback started from 2.75 s right after the shaded light brown region. Shaded cyan regions indicate that the LHCD power was saturated. Magenta dotted lines represent the power command limits of the LHCD power controller, while green dashed lines denote the power request limits of the kinetic controller.

With the given control setup, the performance of each kinetic controller is first assessed by closing the loop on the identified linear two-time-scale model, simply called the ARTAEMIS model [7], which is thus used as a linear plasma simulator. The simulation results are shown in figure 7, indicating that all the controllers can achieve the effective

tracking of  $\beta_p$ ,  $li$ ,  $q_0(= \frac{1}{i_0})$  and  $P_{\text{LHCD}}$ , despite the presence of artificially prescribed disturbances. In the nominal cases, the IMC controller outperforms that of the LQI and  $\mathcal{H}_\infty$  controllers in both  $\beta_p$ ,  $li$  and  $q_0$  tracking, because its design primarily focusses on the fast integral control. In the situations with virtual disturbances exhibiting linear piecewise

curves from 4.5 to 8 s as illustrated in the bottom panels of figures 7(b), (d) and (f), IMC has the best robustness in  $\beta_p$  and li tracking due to its fast integral control, while LQI and  $\mathcal{H}_\infty$  have better robustness than IMC in  $q_0$  tracking because their designs account for the effect of slow plasma eigenmodes.

### 5.5. Closed-loop control experiment

In the closed-loop control experiment, the performance of the two-time-scale cascade kinetic control scheme is further evaluated by tracking a plasma kinetic parameter and the coupled LHCD power simultaneously on the EAST tokamak.

The control of  $\beta_p$  using the IMC tuning rule was performed experimentally in EAST shot #95195, with the feed-forward and feedback gains shown in table 1. A total of five targets, consistent with those used in the ARTAEMIS simulations, were tracked, sequentially 1.75, 1.90, 1.70, 1.85 and 1.80. Figures 8(a) and (b) depict the evolution of  $\beta_p$  and the coupled LHCD power. Evidently, all the targets for  $\beta_p$  and  $P_{\text{LHCD}}$  were achieved using the cascade two-time-scale kinetic control scheme, despite the presence of the large measurement noise in  $\beta_p$ , except during the period [3.6, 4.8] s, when the LHCD actuator had an exceptional fault and was saturated to an upper limit lower than the expected value 2.5 MW. The control of  $\beta_p$  using the  $\mathcal{H}_\infty$  kinetic controller was carried out in shot #95197, whose tuning parameters are listed in table 1. The same SIMC PI power feedback controller was cascaded with the  $\mathcal{H}_\infty$  kinetic controller while the same set of  $\beta_p$  targets were prescribed. The evolution of  $\beta_p$  and  $P_{\text{LHCD}}$  are shown in figures 8(c) and (d). Although all the targets were achieved,  $\beta_p$  exhibits an oscillatory trend and the tracking performance is not as good as in shot #95195, because of the  $\beta_p$  measurement noise and the LHCD power saturation. Comparing these two discharges, one can conclude that the IMC controller performs slightly better than the  $\mathcal{H}_\infty$  controller in the noise-corrupted experimental environment. This is consistent with the ARTAEMIS simulation result.

The control of li using the IMC controller was performed in shot #95196, where two targets were prescribed, i.e. 1.07 and 0.99 and the IMC kinetic controller gains for li are listed in table 1. The same LHCD power feedback control algorithm and measurement preprocessing were used. The evolution of li and  $P_{\text{LHCD}}$  are shown in figures 8(e) and (f). Analogous to  $\beta_p$  control, the signal-to-noise ratio on li is still very large and the use of the moving average filter on li and  $P_{\text{LHCD}}$  turns out to be effective. As shown in figure 8(e), the first target was achieved with some oscillations, due to the presence of measurement noise and model uncertainties. Between 3.0 and 3.5 s, the reference trajectory linearly dropped from 1.07 to 0.99 and the li controller was able to track the reference trajectories with some oscillations, until the LHCD power saturated at 2.3 MW. After 3.38 s, due to the power saturation, the second target could not be reached. As shown in figure 8(f), the LHCD power was precisely tracked via the outer-loop SIMC PI power feedback controller. One can notice that the attractive domain for li control is fairly narrow if only involving the

LHCD power as the control actuator for li tracking. In addition, the measurement fault of the magnetic probes mounted at the plasma boundary is responsible for the unphysical linear drift of li, thus leading to the enhanced control difficulty. Involving more actuators such as the NBI systems is likely to broaden the attractive control region for li. Furthermore, it is anticipated that the removal of the measurement drift arising from the magnetic probe inaccuracy should make the li control more tractable.

## 6. Conclusion and outlook

A two-layer cascade control scheme has been proposed for plasma kinetic control in advanced tokamak scenarios. This control scheme is composed of an inner-layer with a set of alternate controllers to track plasma kinetic parameters of interest, and an outer-layer to preprocess the equilibrium measurements, compensate actuation saturations and track the requested additional heating powers. Taking advantage of the timescale separation property of the kinetic and additional power dynamics evolutions on the EAST tokamak, the kinetic control scheme uses two sampling frequencies, with the inner-layer at 50 Hz and the outer-layer at 1000 Hz. Even though the design of all these real-time kinetic feedback algorithms is based on a linear model identified from the sampled simulation/experimental data, the techniques can straightforwardly be extrapolated to cover those linear models obtained from the first-principles plasma theory. For comparison, three alternative kinetic controllers, the  $\mathcal{H}_\infty$ , LQI and observer-based IMC, are synthesized from the same reduced model, which are subsequently evaluated and compared in closed-loop METIS simulations. These nonlinear simulation results suggest that the proposed kinetic controllers can achieve the prescribed control targets of  $\beta_p$ ,  $\Omega_\phi$  and  $T_{e,0}$  using the LHCD and ICRH powers simultaneously with comparable levels of performance and robustness, which are intimately related to the tuning parameters of each algorithm. This new control scheme has then been implemented into the EAST PCS using the EMC toolbox. Preliminary experiments on the EAST tokamak show that  $\beta_p$ , li and  $P_{\text{LHCD}}$  can successfully be tracked with two simple kinetic controllers, IMC and  $\mathcal{H}_\infty$ , with a 10 ms time-horizon moving average filter and a cascade SIMC PI power tracker. We conclude, from our simulations and initial experiments, that for an intrinsically stable SISO plasma control problem, it is advisable to start with an IMC controller tuned experimentally, as it is proven effective and easy to design; for an uncertain MIMO plasma control problem, the  $\mathcal{H}_\infty$  robust kinetic controller is suggested because its design primarily focusses on enabling sufficient robustness against model uncertainties and meanwhile, its tuning is not very complicated.

In the future, extensive experimental tests by involving more actuators and measurements, for example, the co-current NBI systems and the polarimeter/interferometer diagnostics are foreseen. It would also be interesting to implement adaptive laws to refine the controller parameters in real-time based

on the sampled input–output measurements. Furthermore, coordinating a set of local kinetic controllers for different operating points using gain scheduling can be explored easily under the proposed kinetic control scheme.

### Data availability statement

The data that support the findings of this study are available upon reasonable request from the authors.

### Acknowledgments

This work has been carried out within the framework of the EUROfusion Consortium and has received funding from the Euratom research and training programme 2014–2018 and 2019–2020 under Grant Agreement No. 633053. The views and opinions expressed herein do not necessarily reflect those of the European Commission. This work was supported in part by the China Scholarship Council (CSC), the Excellence Program of Hefei Science Center CAS 2019HSC-UE013, the National Natural Science Foundation of China (No. 11805236) and the National MCF Energy R&D Program of China (No. 2018YFE0302100).

### Appendix A. $\mathcal{H}_\infty$ control design

Our  $\mathcal{H}_\infty$  robust control problem is to synthesize a feedback controller using the reduced model  $G_r(s)$  derived in equation (6) via the mixed-sensitivity  $\mathcal{H}_\infty$  norm optimization [31, 35]. First of all, assuming the to-be-designed controller as  $K_{r,\text{HINF}}(s)$ , we calculate the sensitivity function  $S_r(s) = (I + G_r(s)K_{r,\text{HINF}}(s))^{-1}$ , which maps the control errors from the reference setpoints or the output disturbances. Next, we design the proper weighting matrices  $W_{\text{HINF},S}(s)$  and  $W_{\text{HINF},KS}(s)$  to shape the sensitivity function  $S_r(s)$  and  $K_{r,\text{HINF}}(s)S_r(s)$ , respectively. Then, using the linear matrix inequalities (LMIs) optimization technique [35] and the YALMIP toolbox for MATLAB, the controller  $K_{r,\text{HINF}}(s)$  for  $G_r(s)$  is synthesized by minimizing the  $\mathcal{H}_\infty$  norm of the mixed-sensitivity function  $T_{z_w,\text{HINF}} = [W_{S,\text{HINF}}S_r \quad W_{KS,\text{HINF}}K_{r,\text{HINF}}S_r]$ . After the inverse singular vector transformation, the  $\mathcal{H}_\infty$  robust feedback controller for the plant  $G(s)$  is expressed as  $K_{\text{HINF}}(s) = M_u K_{r,\text{HINF}}(s) M_y$ , where  $M_y$  and  $M_u$  are given in section 2.2. Therefore, the feedback outputs are computed as  $u_{\text{fb},\mathcal{H}_\infty} = K_{\text{HINF}}(s)(y_m - y + y_{\text{aw}})$ ,  $u_{\text{fb}} \in \mathbb{R}^{n_u}$ ,  $y_m, y, y_{\text{aw}} \in \mathbb{R}^{n_y}$ , where  $y$  denotes the measured controlled variables and  $y_{\text{aw}}$  are the anti-windup components [35]. Combining constant feedforwards  $u_m$  and the feedback outputs yields the kinetic control commands as  $u_{\mathcal{H}_\infty} = u_{\text{fb},\mathcal{H}_\infty} + u_m$ .

### Appendix B. LQI control design

Given a reduced kinetic model equation (6), we show here briefly how to design an LQI kinetic controller.

#### B.1. Feedforward design

The state reference  $x_m$  and the input reference  $u_m$  are obtained by solving the reduced model  $G_r(s)$  at steady-state, i.e.  $0 = A_r x_m + B_r u_m, y_m = C_r x_m$ , as:

$$\begin{bmatrix} x_m \\ u_m \end{bmatrix} = \begin{bmatrix} A_r & B_r \\ C_r & 0 \end{bmatrix}^{-1} \begin{bmatrix} 0 \\ I \end{bmatrix} y_m \quad (\text{B.1})$$

where  $y_m$  represents the controlled output reference.

#### B.2. Luenberger observer

The LQI control requires the knowledge of system states that may not be measurable in plasma experiments. However, an observer can be designed to estimate them if the system is observable. In our study, a simple Luenberger observer is employed as:

$$\dot{\hat{x}} = A_r \hat{x} + B_r u + L(y - C_r \hat{x}) \quad (\text{B.2})$$

where  $u, y$  and  $\hat{x}$  are the measured inputs, the measured outputs and the state estimates, respectively.  $L$  is a tuning gain matrix chosen to artificially place the observer eigenvalues such that the state estimates can converge exponentially faster than the system evolution.

#### B.3. Feedback design

The LQI feedback commands  $u_{\text{fb,LQI}}$  are computed by minimizing a cost function  $J_{\text{fb,LQI}}$  that penalizes both the state errors, the output error integrals and the control inputs as:

$$\arg \min_{u_{\text{fb,LQI}}} J_{\text{fb,LQI}} = \frac{1}{2} \int_{t_0}^{\infty} (e_a^T Q e_a + u_{\text{fb,LQI}}^T R u_{\text{fb,LQI}}) dt \quad (\text{B.3})$$

where  $Q^T = Q \geq 0$  is a weighting matrix for the state errors  $x_{\text{err}} = x_m - \hat{x}$  and the output error integrals  $z = \int_0^t (y_m - y) dt$ .  $R^T = R > 0$  is a weighting matrix for the control inputs.  $e_a = [x_{\text{err}}^T, z^T]^T$  and  $u_{\text{fb,LQI}}$  represents the optimal feedback commands, parameterized as  $u_{\text{fb,LQI}} = -K_{\text{fb,LQI}} e_a$ . The feedback synthesis objective is to obtain an optimal gain matrix  $K_{\text{fb,LQI}}$  that minimizes equation (B.3). To compute  $K_{\text{fb,LQI}}$ , we first augment the plasma plant with a vector of additional states  $z$  as:

$$\begin{bmatrix} \dot{x} \\ \dot{z} \end{bmatrix} = M_A \begin{bmatrix} x \\ z \end{bmatrix} + M_B u + M_W y_m \quad (\text{B.4})$$

where

$$M_A = \begin{bmatrix} A & 0 \\ -C & 0 \end{bmatrix}, M_B = \begin{bmatrix} B \\ 0 \end{bmatrix}, M_W = \begin{bmatrix} 0 \\ I \end{bmatrix}. \quad (\text{B.5})$$

Given the augmented system matrices, the optimal gain matrix is then expressed as  $K_{\text{fb,LQI}} = -R^{-1} M_B^T P$ , where  $P$  is a symmetric positive-definite matrix that satisfies an algebraic Riccati equation [31] as:

$$P M_A + M_A^T P - P M_B R^{-1} M_B^T P + Q = 0. \quad (\text{B.6})$$

The optimal feedback commands are thus calculated as  $u_{fb,LQI} = K_{fb,LQI}(y_m - y + y_{aw})$ ,  $u_{fb,LQI} \in \mathbb{R}^{n_u}$ ,  $y_m, y, y_{aw} \in \mathbb{R}^{n_y}$ , where  $y_{aw}$  are the anti-windup compensated components [35]. Combining the feedforward  $u_m$  and feedback commands  $u_{fb,LQI}$ , the LQI control inputs are  $u_{LQI} = u_{fb,LQI} + u_m$ .

## Appendix C. Observer-based IMC control design

Having obtained a reduced kinetic model equation (6), we show here briefly how to design an observer-based IMC kinetic controller.

### C.1. State and disturbance estimation

To estimate the system states and disturbances, we assume constant system disturbances, i.e.  $\dot{d} = 0$  [49], and extend the reduced model equation (6) as:

$$\begin{aligned} \dot{x} &= A_r x + B_r u + B_d d \\ \dot{d} &= 0 \\ y &= C_r x + C_d d \end{aligned} \quad (C.1)$$

where  $x \in \mathbb{R}^{n_x}$ ,  $u \in \mathbb{R}^{n_u}$ ,  $d \in \mathbb{R}^{n_d}$ ,  $y \in \mathbb{R}^{n_y}$  are respectively the states, the inputs, the disturbances and the outputs.  $B_d$  and  $C_d$  are coefficient matrices to be determined. To guarantee the detectability of the augmented plasma model, we must prescribe the matrices  $(B_d, C_d)$  to satisfy the condition  $\text{rank} \begin{bmatrix} A & B_d \\ C & C_d \end{bmatrix} = n_x + n_d$ . By setting  $B_d = 0, C_d = I$ , the disturbances at the output are observed, while by prescribing  $B_d = B_p, C_d = 0$ , the disturbances at the input are estimated. In this study, we choose the former setup, i.e.  $B_d = 0, C_d = I$ .

Combining the states  $x$  and the disturbances  $d$  into a state vector, i.e.  $X = [x^T, d^T]^T$ , we formulate the extended model in a compact form as:

$$\begin{aligned} \dot{X} &= A_e X + B_e u \\ y &= C_e X \end{aligned} \quad (C.2)$$

where  $A_e = \begin{bmatrix} A_r & B_d \\ 0 & C_d \end{bmatrix}$ ,  $B_e = \begin{bmatrix} B_r \\ 0 \end{bmatrix}$ ,  $C_e = [C_r \quad C_d]$ .

The Luenberger observer is then expressed as:

$$\begin{aligned} \dot{\hat{X}} &= A_e \hat{X} + B_e u + L(y - \hat{y}) \\ \hat{y} &= C_e \hat{X} \end{aligned} \quad (C.3)$$

where  $\hat{X} = [\hat{x}^T, \hat{d}^T]^T$  represents the estimate of  $X$  while  $\hat{y}$  denotes the estimate of  $y$ .  $L$  is a gain matrix that can be tuned by placing the eigenvalues of the error dynamics.

### C.2. State feedback stabilization

With the observer, the states and disturbances can therefore be estimated in real-time. To stabilize the plasma plant, we use the reduced model to design a state feedback controller, parameterized as  $u_{sf} = -F_{sf} \hat{x}$ .  $F_{sf}$  is a static gain matrix to place the system poles to desirable stable region (with negative real

eigenvalues), which is a crucial trick to control unstable or marginally stable plasma dynamics [49].

### C.3. Offset-free internal model control

The offset-free IMC control inputs comprise the standard IMC control component  $u_{sIMC}$  for disturbance rejection, the state feedback component  $u_{sf}$  for state stabilization and the preset feedforward component  $u_m$ , which reads:

$$u_{IMC} = u_{sIMC} - u_{sf} + u_m \quad (C.4)$$

where  $u_{sIMC} = Q_{Youla}(s)(r - M\hat{d})$ , in which the to-be-designed terms include a stable transfer matrix  $Q_{Youla}(s)$  and a static gain matrix  $M$ . To design them, we formulate the stabilized plasma dynamic model  $G_{sf}(s)$  and the disturbance dynamic model  $G_{dist}(s)$  as:

$$G_{sf}(s) = \left[ \begin{array}{c|c} A_r - F_{sf} B_r & B_r \\ \hline C_r & 0 \end{array} \right] \quad (C.5)$$

$$G_{dist}(s) = \left[ \begin{array}{c|c} A_r - F_{sf} B_r & B_d \\ \hline C_r & C_d \end{array} \right]. \quad (C.6)$$

IMC requires the steady-state gain of the open-loop transfer matrix to be an identity matrix, i.e.  $G_{sf}(0)Q(0) = I$ . For simplicity, we design  $Q(s) = F(s)G_{sf}(0)^\dagger = -F(s) \left( C_r (A_r - F_{sf} B_r)^{-1} B_r \right)^\dagger$ , where  $\dagger$  represents the pseudoinverse. The lowpass filter transfer matrix  $F(s)$  is expressed as  $F(s) = \text{diag}(f_1(s), \dots, f_{n_u}(s))$ ,  $f_k(s) = \frac{1}{(\lambda_k s + 1)^k}$ ,  $k = 1, 2, \dots, n_u$ , in which  $\lambda_i$  are free parameters to be tuned [49]. The static gain matrix  $M$  is designed as  $M = G_{dist}(0) = -C_r (A_r - F_{sf} B_r)^{-1} B_d + C_d$ .

## Appendix D. SIMC PI actuation control design

We assume that the additional heating system dynamics can be modelled as a set of first-order transfer functions with time-delay as:

$$G_{outer,i}(s) = \frac{k_i}{\tau_i s + 1} e^{-\theta_i s}, i \in \{\text{ICRH, LHCD}\} \quad (D.1)$$

where  $i$  is an integer that refers to a particular H&CD actuator,  $k_i$  denoting the steady-state gain for the  $i$ th actuator,  $\tau_i$  the characteristic time for the  $i$ th actuator, while  $\theta_i$  represents the time delay for the  $i$ th actuator.  $G_{outer,i}(s)$  is a transfer function for the  $i$ th actuator determined by three model parameters, i.e.  $k_i$ ,  $\tau_i$  and  $\theta_i$ .

Once the actuator dynamics is characterized by a simple model structure as shown in equation (D.1), we can then use a tuning rule based on the internal model principle to design an outer-layer PI actuator controller [31]. We define  $u_{inner,i}(t)$  as the command requested by the inner-layer kinetic controller for the  $i$ th actuator controller and  $u_{mea,i}(t)$  as the corresponding measured actuation for the  $i$ th actuator. The actuation tracking error  $e_{outer,i}$  is thus computed as  $e_{outer,i} = u_{inner,i}(t) - u_{mea,i}(t)$ .

The PCS commands requested by the  $i$ th actuator controller  $u_{\text{outer},i}(t)$  are then expressed as:

$$u_{\text{outer},i}(t) = -K_{p,i}e_{\text{outer},i} - K_{I,i} \int_0^t e_{\text{outer},i} dt + u_{\text{offset},i}, i \in \{\text{ICRH, LHCD}\} \quad (\text{D.2})$$

in which

$$\begin{aligned} K_{p,i} &= \frac{\tau_i}{k_i(\tau_{c,i} + \theta_i)} \\ K_{I,i} &= \frac{K_{p,i}}{\tau_{I,i}} \\ \tau_{I,i} &= \min\{\tau_i, (\tau_{c,i} + \theta_i)\} \end{aligned} \quad (\text{D.3})$$

where  $K_{p,i}$  and  $K_{I,i}$  are the proportional and integral gains for the  $i$ th actuator, respectively.  $u_{\text{offset},i}$  denotes the  $i$ th reference value around which the actuator model  $G_{\text{outer},i}(s)$  is identified.  $\tau_{c,i}$  is a tuning parameter for the  $i$ th actuator, which provides a trade-off between control performance and robustness against disturbances. More precisely, increasing  $\tau_{c,i}$  can result in the growth of the response time but the control robustness can thus be improved, and it is suggested to have  $\tau_{c,i} \geq \theta_i$ . We emphasize that, in order to guarantee the actuation tracking performance, the sampling time for the actuator controllers (typically at 1 ms on the EAST tokamak) should be smaller than the characteristic time for each H&CD systems and far less than that for the kinetic controller ( $\sim \tau_E$ ).

## ORCID iDs

S Wang  <https://orcid.org/0000-0002-9666-1158>  
 E Witrant  <https://orcid.org/0000-0002-2026-8915>  
 Q P Yuan  <https://orcid.org/0000-0003-4292-1302>  
 L Zeng  <https://orcid.org/0000-0003-4968-1401>

## References

- [1] Wesson J and Campbell D J 2011 *Tokamaks* vol 149 (Oxford: Oxford University Press)
- [2] Freidberg J P 2008 *Plasma Physics and Fusion Energy* (Cambridge: Cambridge University Press)
- [3] Wolf R 2002 *Plasma Phys. Control. Fusion* **45** R1
- [4] Joffrin E 2007 *Plasma Phys. Control. Fusion* **49** B629
- [5] Doyle E et al 2006 *Plasma Phys. Control. Fusion* **48** B39
- [6] Witrant E, Joffrin E, Brémond S, Giruzzi G, Mazon D, Barana O and Moreau P 2007 *Plasma Phys. Control. Fusion* **49** 1075
- [7] Moreau D et al 2013 *Nucl. Fusion* **53** 063020
- [8] Boyer M, Andre R, Gates D, Gerhardt S, Menard J and Poli F 2017 *Nucl. Fusion* **57** 066017
- [9] Barton J E 2015 Physics-model-based optimization and feedback control of the current profile dynamics in fusion tokamak reactors *PhD Dissertation* Lehigh University
- [10] Mavkov B 2017 Control of coupled transport in tokamak plasmas *PhD Thesis*
- [11] Moreau D et al 2003 *Nucl. Fusion* **43** 870
- [12] Mazon D et al 2003 *Plasma Phys. Control. Fusion* **45** L47
- [13] Boyer M D, Barton J, Schuster E, Luce T C, Ferron J R, Walker M L, Humphreys D A, Penaflor B G and Johnson R D 2013 *Plasma Phys. Control. Fusion* **55** 105007
- [14] Moreau D et al 2008 *Nucl. Fusion* **48** 106001
- [15] Barton J E et al 2012 *Nucl. Fusion* **52** 123018
- [16] Barton J E, Besseghir K, Lister J and Schuster E 2015 *Plasma Phys. Control. Fusion* **57** 115003
- [17] Maljaars E, Felici F, De Baar M, van Dongen J, Hogewijj G, Geelen P and Steinbuch M 2015 *Nucl. Fusion* **55** 023001
- [18] Maljaars E et al 2017 *Nucl. Fusion* **57** 126063
- [19] Moreau D, Wang S, Witrant E, Qian J and Yuan Q 2021 Model-predictive kinetic control experiments on EAST *Proc. 28th IAEA Fusion Energy Conf. (IAEA)*
- [20] Vu N T et al 2017 *Fusion Eng. Des.* **123** 624–7
- [21] Argomedeo F B, Witrant E, Prieur C, Brémond S, Nouailletas R and Artaud J F 2013 *Nucl. Fusion* **53** 033005
- [22] Mavkov B et al 2018 *Nucl. Fusion* **58** 056011
- [23] Mameche H, Witrant E and Prieur C 2019 Nonlinear PDE-based control of the electron temperature in H-mode tokamak plasmas 2019 *IEEE 58th Conf. on Decision and Control (CDC)* (IEEE) pp 3227–32
- [24] Kim S and Lister J 2012 *Nucl. Fusion* **52** 074002
- [25] Huang Y et al 2020 *Nucl. Fusion* **60** 076023
- [26] Artaud J et al 2018 *Nucl. Fusion* **58** 105001
- [27] Moreau D et al 2011 *Nucl. Fusion* **51** 063009
- [28] Moreau D et al 2015 *Nucl. Fusion* **55** 063011
- [29] Ljung L 1995 *System Identification Toolbox: User's Guide* (Natick, MA: MathWorks Incorporated)
- [30] Reyhanoglu M, van der Schaft A, McClamroch N H and Kolmanovsky I 1999 *IEEE Trans. Autom. Control* **44** 1663–71
- [31] Skogestad S and Postlethwaite I 2007 *Multivariable Feedback Control: Analysis and Design* vol 2 (New York: Wiley)
- [32] Ferron J, Walker M, Lao L, John H S, Humphreys D and Leuer J 1998 *Nucl. Fusion* **38** 1055
- [33] Baylor L R, Burrell K, Groebner R, Houlberg W A, Ernst D, Murakami M and Wade M R 2004 *Phys. Plasmas* **11** 3100–5
- [34] Liu H et al 2014 *Rev. Sci. Instrum.* **85** 11D405
- [35] Wang S, Witrant E and Moreau D 2021 *Fusion Eng. Des.* **162** 112071
- [36] Nouailletas R et al 2019 WEST magnetic control 2019 *IEEE 58th Conf. on Decision and Control (CDC)* (IEEE) pp 3214–19
- [37] Young P C and Willems J 1972 *Int. J. Control* **15** 961–79
- [38] Anderson B D and Moore J B 2007 *Optimal Control: Linear Quadratic Methods* (Courier Corporation)
- [39] Hassen S S, Heurs M, Huntington E H, Petersen I R and James M 2009 *J. Phys. B: At. Mol. Opt. Phys.* **42** 175501
- [40] ElMadany M M and Abduljabbar Z S 1999 *Veh. Syst. Dyn.* **32** 479–97
- [41] Gurung N, Bhattarai R and Kamalasadana S 2017 Optimal linear-quadratic-integral controller design for doubly-fed induction generator 2017 *IEEE Power & Energy Society General Meeting* (IEEE) pp 1–5
- [42] Vail P J, Boyer M D, Welander A S and Kolemen E 2019 *Plasma Phys. Control. Fusion* **61** 035005
- [43] Garcia C E and Morari M 1982 *Ind. Eng. Chem. Process. Des. Dev.* **21** 308–23
- [44] Saxena S and Hote Y V 2012 *IETE Tech. Rev.* **29** 461–72
- [45] Harnefors L and Nee H P 1998 *IEEE Trans. Ind. Appl.* **34** 133–41
- [46] Narayanan N L, Krishnaswamy P and Rangaiah G 1997 *Chem. Eng. Sci.* **52** 3067–74
- [47] Yazdani M and Mehrizi-Sani A 2014 *IEEE Trans. Energy Convers.* **29** 873–81
- [48] Gruber O, Lackner K, Pautasso G, Seidel U and Streibl B 1993 *Plasma Phys. Control. Fusion* **35** B191
- [49] Pannocchia G and Heath W P 2020 *Automatica* **122** 109270
- [50] Liu H et al 2016 *Rev. Sci. Instrum.* **87** 11D903